ACS APPLIED MATERIALS & INTERFACES

Research Article

www.acsami.org

A Novel Carboxyethyltin Functionalized Sandwich-type Germanotungstate: Synthesis, Crystal Structure, Photosensitivity, and Application in Dye-Sensitized Solar Cells

Xiaojing Sang,[†,§] Jiansheng Li,[†,§] Lancui Zhang,*[,‡] Zanjiao Wang,[‡] Weilin Chen,*[,†] Zaiming Zhu,[‡] Zhongmin Su,[†] and Enbo Wang*[,†]

[†]Key Laboratory of Polyoxometalate Science of Ministry of Education, Department of Chemistry, Northeast Normal University, Changchun, Jilin 130024, China

[‡]School of Chemistry and Chemical Engineering, Liaoning Normal University, Dalian 116029, China

Supporting Information

ABSTRACT: A novel sandwich-type germanotungstate $[C(NH_2)_3]_{10}[Mn_2\{Sn(CH_2)_2COOH\}_2(B\text{-}\alpha\text{-}GeW_9O_{34})_2]\cdot 8H_2O$ (**1**) represents the first single crystalline polyoxometalate (POM) functionalized by open chain carboxyethyltin, which was designed and synthesized in aqueous solution and applied to a dye-sensitized solar cell (DSSC) for the first time. Its photosensitivity was explored through a fluorescence spectrum (FL), surface photovoltage spectrum (SPV), electrochemical method, and solid diffuse spectrum. **1** displays the primary features of sensitizers in DSSCs, and the efficiency of the solar cell is 0.22%. Delightedly, when **1** was employed to assemble a cosensitized solar cell configuration by preparing a **1**-doped TiO_2 electrode and additionally adsorbing N719 dyes, a considerably improved efficiency was achieved through increasing spectral absorption and accelerating electron transport, which is 19.4% higher than that of single N719 sensitization. This result opens up a new way to position different dyes on a single TiO_2 film for cosensitization.

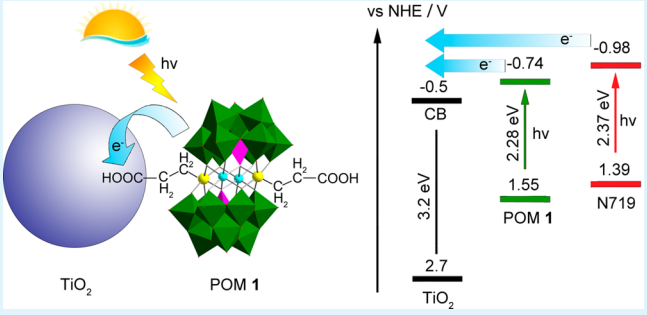

KEYWORDS: *polyoxometalate, carboxyethyltin, photosensitivity, TiO_2, dye-sensitized solar cell*

1. INTRODUCTION

Dye-sensitized solar cells (DSSC)s are a promising advanced photovoltaic technology as low-cost alternatives to conventional silicon-based solar cells.[1] The core component of DSSC is the photosensitizer.[2] Upon light illumination, the vectorial electrons flow from the dye toward the semiconductor and then transport through the mesoporous TiO_2 electrode.[3] Ruthenium sensitizers have shown very impressive solar-to-electric power conversion efficiency, but they are suffering from the restrictions of noble metal.[4,5] Subsequently, organic dyes were developed as metal-free complexes without a limit of resources, which have good flexibility for tailoring, but their stability is poor.[6−8] Semiconductor quantum dots received widespread attention due to their spectrum absorption tunability by the control of size and composition, but light corrosion limited their application.[9] The development of new sensitizers for DSSCs is very important to improve the overall efficiency of the cell and reduce the production cost. Polyoxometalates (POMs), as a class of metal−oxygen cluster compounds based on abundant element composition, play important roles in diverse disciplines involving catalysis, materials science, medicine, and analytical chemistry due to their fascinating structural, catalytic, photophysical, magnetic, and electrochemical properties.[10−27] POMs have been found to exhibit molecular semiconductor-like properties[28,29] and could be capable of acting as an extremely valuable building block in photovoltaics. In addition, POMs could be explored as tunable chromophores by accommodating multiple transitional metals. It will be a new breakthrough to explore POMs-based sensitizers on account of their abundant element composition and high stability. However, there were few reports on this. Su et al. put forward a series of organoimido-substituted hexamolybdate dyes for TiO_2-based solar cells by theoretical calculations. But there was no relevant experimental research about these dyes.[30] The major challenges in exploring POMs-based dyes are the energy level regulation of the lowest unoccupied molecular orbital (LUMO)[3] and the anchoring groups to strongly bind the dye onto the semiconductor surface.[31] Previously, some classic POMs were usually applied as the electron mediator in photovoltaics to accelerate the electron transmission and suppress the carrier recombination on the semiconductor surface through compositing with TiO_2 or ZnO due to their lower LUMO levels than the semiconductors.[32−36] On the other hand, it is worth noting that the electron characteristic

Received: February 27, 2014
Accepted: April 23, 2014
Published: April 23, 2014

and redox property of POMs could be adjusted by control of the structure or composition, which provides a basis for exploring a POM-based sensitizer. We have been working on the photosensitivity of POMs, and the preliminary study which was carried out from the energy level regulation shows the feasibility.[37]

Organotin decorated POMs[38] are a class of fascinating POM derivatives in POM-based organic−inorganic functionalization.[39−45] The charge density of oxygen ions on the surface of POMs would change after organotin decorating,[41] which could adjust the electronic characteristic and redox properties of POMs. We have successfully obtained five ring carboxyethyltin decorated POM derivatives by introducing a carboxyl group into the POM skeleton.[46−49] Herein, we synthesized the first single crystal sandwich-type germanotungstates functionalized by open chain carboxyethyltin (**1**). The carboxylic acid anchoring group could guarantee the loading of POMs on TiO_2 and tight electron coupling. Then we studied its photosensitivity for the first time through FL and SPV spectra, and the detailed investigation of its redox properties by cyclic voltammetry method (CV) and solid diffuse spectrum. Besides, in view of the semiconductor-like nature of **1** and its high thermal stability, a **1**-doped TiO_2 electrode was prepared by introducing the **1**-loaded TiO_2 composite (denoted as **1**T) to the photoanode. Then a **1** and N719 cosensitized solar cell configuration was constructed by further N719 sensitization. The synergistic effect of **1** and N719 finally boosted the efficiency of the solar cell as compared to a single N719-based one through increasing the spectral absorption and accelerating electron transport.

2. EXPERIMENTAL SECTION

2.1. Chemicals and Reagents. $Na_{12}[Mn_4(H_2O)_2(GeW_9O_{34})_2]\cdot 38H_2O$ and $Cl_3Sn(CH_2)_2COOCH_3$ were synthesized according to the reported methods and characterized by IR.[50,51] All other chemicals were purchased commercially and used without further purification.

2.2. Synthesis of $[C(NH_2)_3]_{10}[Mn_2\{Sn(CH_2)_2COOH\}_2(B\text{-}\alpha\text{-}GeW_9O_{34})_2]\cdot 8H_2O$ (1). $Na_{12}[Mn_4(H_2O)_2(GeW_9O_{34})_2]\cdot 38H_2O$ (1.14 g, 0.2 mmol) was dissolved in 15.0 mL of water to form solution A, and $Cl_3Sn(CH_2)_2COOCH_3$ (0.24 g, 0.077 mmol) was dissolved in 10.0 mL of water to form solution B. Then, solution B was added dropwise to solution A. The resulting solution was stirred at 80 °C for about 2 h. After cooling to room temperature, 4 mL of 1.0 mol L^{-1} $C(NH_2)_3Cl$ and 3.86 g of KCl were added to the mixture, and yellow precipitate was immediately obtained. The crude product was collected by filtration and recrystallized with 15.0 mL of water. Yellow columnar-shaped single crystals were isolated by slow evaporation for 2 weeks (yield 53% based on Ge). Anal. Calcd for $C_{16}H_{86}N_{30}Mn_2Sn_2Ge_2W_{18}O_{80}$ (**1**) (%): C, 3.32; H, 1.50; N, 7.27; Mn, 1.90; Sn, 4.11; Ge, 2.51; W, 57.24. Found (%): C, 3.38; H, 1.58; N, 7.14; Mn, 1.98; Sn, 4.19; Ge, 2.60; W, 57.18. IR (solid KBr pellet ν/cm^{-1}): 3416(s), 2930(w), 2853(w), 1668(s), 1250(s), 953(m), 862(s), 785(s), 747(s), 520(w), 459(w).

2.3. Preparation of $[DODA]_{10}[Mn_2\{Sn(CH_2)_2COOH\}_2(B\text{-}\alpha\text{-}GeW_9O_{34})_2]$. **1** (0.05782g, 0.01 mmol) was dissolved in 20 mL of distilled water, and to this aqueous solution was added a 30 mL chloroform solution of DODACl (0.44g, 0.15 mmol) dropwise with stirring. After stirring for 4 h at room temperature, the organic phase was separated and evaporated to dryness. The target product was dried under vacuum conditions. A **1**-absorbed TiO_2 electrode was prepared by immersion of a bare TiO_2 electrode into a dichloromethane solution of 0.5 mM $[DODA]_{10}[Mn_2\{Sn(CH_2)_2COOH\}_2(B\text{-}\alpha\text{-}GeW_9O_{34})_2]$ for 4 h and then assembled into DSSC by a similar method with a N719-based solar cell in the following.

2.4. Preparation of 1T. To a solution of **1** (0.04 g) in DMSO (20 mL) at 120 °C was added a P25 (0.2 g) suspension (10 mL DMSO) dropwise with vigorous stirring. After 2 h, the obtained mixture was centrifugally separated, washed with anhydrous ethanol and then dried at 80 °C for 8 h. Then the obtained **1**T was mixed with P25 with a mass fraction of 2.0% (denoted as **1**T/TiO_2) and then was used to fabricate the photoanode.

2.5. Solar Cell Fabrication. FTO conductive glass was ultrasonically cleaned with surfactant, isopropanol, and ethanol. The clean substrate was then coated with TiO_2 paste with **1**T/TiO_2 and without **1**T by screen printing[52] and sintered at 400 °C for 30 min. Subsequently, the resulting films were post-treated in 40 mmol L^{-1} $TiCl_4$ solution for 30 min at 70 °C and calcined in the air at 400 °C for 30 min again. When cooled to 80 °C, the film was immersed in N719 ethanol solution for 24 h. Then the dye-covered electrodes were covered with platinum mirrors as counter electrodes. The electrolyte is composed of 0.1 mol L^{-1} LiI, 0.05 mol L^{-1} I_2, 0.6 mol L^{-1} 1,2-dimethyl-3-propylimidazolium iodide, and 0.5 mol L^{-1} 4-*tert*-butylpyridine in 3-methoxypropionitrile.

2.6. Characterization Methods. Elemental analyses for C, H, and N were performed on a Perkin−Elmer 2400 CHN elemental analyzer. The elemental analyses of Ge, Mn, Sn, and W were analyzed on a Plasma-Spec-II ICP atomic emission spectrometer. IR spectra were recorded using KBr pellets on a Bruker AXS TENSOR-27 FTIR spectrometer in the range of 4000−400 cm^{-1}. TG analyses were performed on a Pyris Diamond TG−DTA thermal analyzer at a heating rate of 10 °C min^{-1} from 35 to 800 °C. X-ray powder diffraction data was collected on a Bruker AXS D8 Advance diffractometer using Cu Kα radiation (λ = 1.5418 Å) in the 2θ range of 5−60° with a step size of 0.02°. Cyclic voltammograms were recorded on a CHI601D Electrochemical Workstation (Shanghai Chenhua Instrument Corp., China), using a glassy carbon electrode as the working electrode, a Pt wire as the counter electrode, and a Ag/AgCl reference electrode. A NaAc/HAc buffer solution with a pH of 6.5 was used as the supporting electrolyte. The diffuse reflectivity spectra were collected on a UV-2600 SHIMADZU UV−vis spectrophotometer in reflectance mode, which was measured from 200 to 800 nm using barium sulfate ($BaSO_4$) as a standard with 100% reflectance. The fluorescence spectra were measured on the FL900/FS920 steady-state fluorescence spectrometer. The fluorescence emission band is located at 392 nm upon excitation at 247 nm. The surface photovoltage spectroscopy measurement is carried out on a lab-made instrument, which constitutes a source of monochromatic light, a lock-in amplifier (SR830-DSP) with a light chopper (SR540), and a photovoltaic cell. A 500 W xenon lamp (CHFXQ500 W, Global xenon lamp power) and a double-prism monochromator (Hilger and Watts, D300) provide monochromatic light. The construction of the photovoltaic cell was a sandwich-like structure of ITO−sample−ITO. A Keithley 2400 source meter and a Zolix Omni-300 monochromator equipped with a 500 W xenon lamp were used for photocurrent action spectrum measurements, with a wavelength sampling interval of 10 nm and a current sampling time of 2 s under the full computer control. A model LS1000−4S-AM1.5G-1000W solar simulator (Solar Light Company, USA) in combination with a metal mesh was employed to give an irradiance of 100 mW cm^{-2}. $J-V$ characteristics were obtained by applying a potential bias to a testing cell and measuring dark current and photocurrent with a Keithley 2602 source meter under the full computer control. A metal mask with an aperture area of 0.1598 cm^2 was covered on a testing cell during all measurements. The short-circuit photocurrent densities measured under this solar simulator are well consistent with the integral of IPCEs with the AM1.5G spectrum (ASTMG173−03).

2.7. X-Ray Crystallography. X-ray diffraction data were collected on a Bruker Smart APEXII X-diffractometer equipped with graphite-monochromated Mo Kα radiation (λ = 0.71073 Å). An empirical absorption correction was applied using the SADABS program. The structures were solved by direct methods and refined by the full-matrix least-squares fitting on F^2 using the SHELXTL-97 package.[53] Cell parameters were obtained by the global refinement of the positions of all collected reflections. All the non-hydrogen atoms were refined anisotropically. Hydrogen atoms on C and N atoms were added in calculated positions. Crystal data and structure refinement parameters

of compound **1** are listed in Table 1. Selected bond lengths and angles are listed in Table S1, and hydrogen bonds are given in Table S2. The CCDC reference number is 978867.

Table 1. Crystal and Refinement Data for Compound 1

compound	1
formula	$C_{16}H_{86}N_{30}Mn_2Sn_2Ge_2W_{18}O_{80}$
formula weight/g mol^{-1}	5780.79
wavelength /Å	0.710 73
T/K	298(2)
cryst size/mm	0.14× 0.07 × 0.06
cryst syst	monoclinic
space group	$P2_1/c$
a/Å	12.208(3)
b/Å	17.734(4)
c/Å	24.861(5)
β/deg	115.658(9)
V/Å^3	4852.4(19)
Z	2
D_c /Mg m^{-3}	3.956
μ /mm^{-1}	22.720
$F(000)$	5154
R_{int}	0.1107
R_1 ($I > 2\sigma(I)$)[a]	0.0574
wR_2 (all data)[a]	0.1410
goodness-of-fit on F^2	0.986

[a] $R_1 = \sum||F_o| - |F_c||/\sum|F_o|$; $wR_2 = \sum[w(F_o^2 - F_c^2)^2]/\sum[w(F_o^2)^2]^{1/2}$.

3. RESULTS AND DISCUSSION

3.1. Crystal Structures. Single crystal X-ray diffraction analysis reveals that **1** is composed of one polyoxoanion $[Mn_2\{Sn(CH_2)COOH\}_2(B\text{-}\alpha\text{-}GeW_9O_{34})_2]^{10-}$, 10 isolated $[C(NH_2)_3]^+$, and eight crystal waters moleculars (Figure S1). The polyoxoanion of **1** displays the well-known sandwich-type structural feature. It can be viewed as two B-α-$[GeW_9O_{34}]^{10-}$ units (Figure 1) combined with two $[Sn(CH_2)_2COOH]^{3+}$ moieties and two Mn^{2+} cations sharing corner O atoms of WO_6 octahedra and GeO_4 tetrahedra. The W−O distances are in the range of 1.680(16)−2.445(13) Å. Two Mn^{2+} cations and two $[Sn(CH_2)_2COOH]^{3+}$ moieties were located in the inner and outer positions in the central core of the complex, respectively (see Figure 2). In **1**, each $[Sn(CH_2)_2COOH]^{3+}$

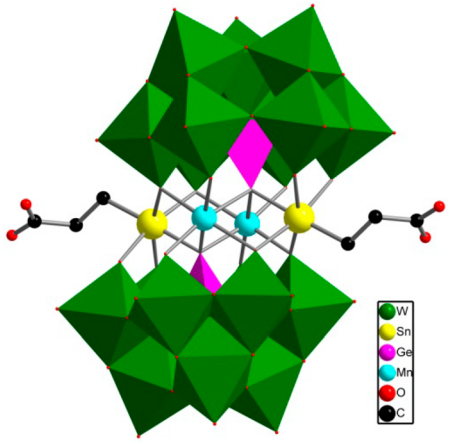

Figure 1. Polyhedral and ball-and-stick representation of the polyoxoanion in **1**.

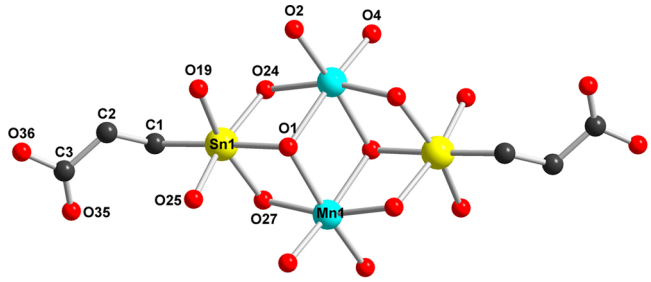

Figure 2. Ball-and-stick representation of the central $\{(SnCH_2CH_2COOH)_2Mn_2O_{14}\}$ fragment of polyoxoanion **1**.

unit links two B-α-$[GeW_9O_{34}]^{10-}$ units via five terminal oxygen atoms from two POMs units, forming hexa-coordinated environments for two Sn centers (Sn1 and its symmetrical equivalent position). The Sn−C distance is 2.11(3) Å, and the Sn−O distances are in the range of 2.093(16)−2.150(15) Å. Each Mn^{2+} ion is six-coordinated by six terminal oxygen atoms derived from two B-α-$[GeW_9O_{34}]^{10-}$ units. The Mn−O distances are in the range of 2.049(14)−2.300(15) Å. Furthermore, the estertin precursor $[Sn(CH_2)_2COOCH_3]^{3+}$ hydrolyzes into carboxyethyltin $[Sn(CH_2)_2COOH]^{3+}$ during the reaction process; such a phenomenon has never been observed in our recent reports on POM-estertin derivatives.[46−49] But the difference is that the original Sn−$O_{carboxyl}$ bond is broken resulting in the cyclic carboxyethyltin converted into a chain structure (see Scheme 1).

Scheme 1. Hydrolysis of Estertin into Open Chain Carboxyethyltin Group during the Synthetic Process of 1

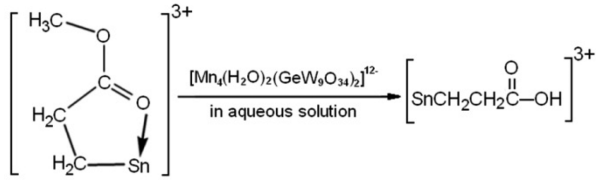

As shown in Figure 2 and Scheme 1, in the $[Sn(CH_2)_2COOH]^{3+}$ unit, there is an exposed carboxyl group. The newly exposed carboxyl-terminal group can link with metal cations or organic groups; that is to say, it can make the POM-carboxyethyltin derivatives further functionalized. This provides a guarantee for the adsorption of POMs on the surface of TiO_2. In the packing arrangement of **1** (Figure S2), the adjacent sandwich-type polyoxoanions are stacked into a 3-D supramolecular framework via the extensive H-bonding interactions.

The powder XRD pattern of compound **1** and its simulated PXRD pattern are shown in Figure S3. Their main peak positions are in good agreement with each other, confirming that the product is a pure phase. The differences in reflection intensity are probably due to preferred orientation in the powder samples. The structure of **1** was further characterized by FTIR shown in Figure S4.

3.2. Photoelectrochemical Characterization. Fluorescence and surface photovoltage spectra were first carried out to study the charge transfer process at the interface of TiO_2 and **1**. Figure 3a shows the fluorescence emission spectra. The aqueous solution of **1** has a fluorescence emission band at 392 nm upon excitation at 247 nm. When a moderate amount of TiO_2 powder was added to the above solution, the emission of **1** with a maximum at 392 nm is very efficiently quenched by

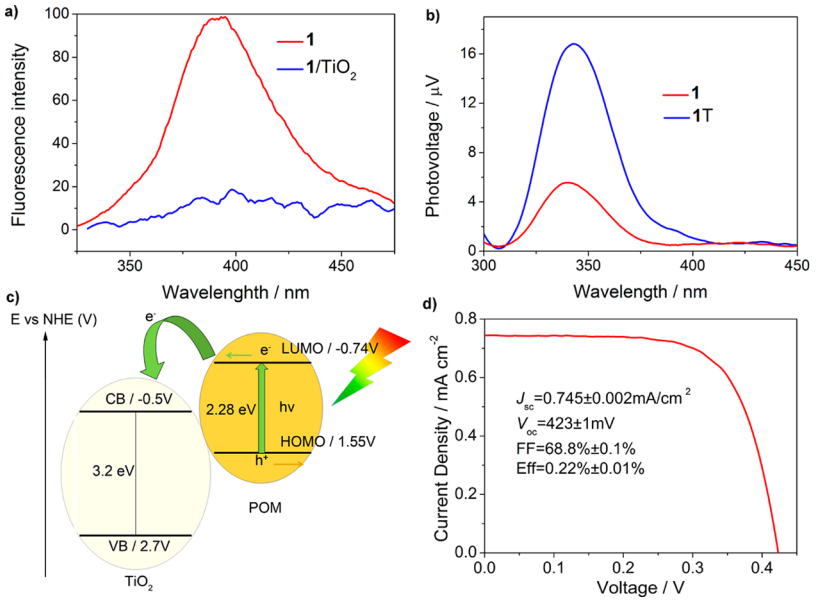

Figure 3. (a) Effect of TiO_2 on the fluorescence emission spectrum of **1** in aqueous solution with the concentration of 5×10^{-6} mol L^{-1}. Red line, no TiO_2 present; blue line, $[TiO_2] = 0.25$g L^{-1}. (b) The surface photovoltage spectrum of compound **1** (red line) and **1**T. (c) The schematic energy level of **1** and TiO_2. (d) The current−voltage curve of **1** sensitized solar cells under AM 1.5 illumination with dimethyldioctadecyl cation (Figure S7) in dichloromethane.

TiO_2, which indicated that the photoinduced electron transmission from **1** to TiO_2 clusters could be established from the fluorescence quenching.[54] Actually, TiO_2 extracted the photoelectrons in **1** due to the higher LUMO of **1** and tight coupling between TiO_2 and **1**. To further confirm this process, we collected an SPV spectrum to characterize the carrier separation and transfer behavior at the interface of TiO_2 and **1**.[55] Figure 3b shows the SPV spectrum of **1** and the **1**T composite. Compound **1** displays significant surface photovoltaic at 340 nm, demonstrating that **1** has a semiconductor nature and would produce effective electron−hole separation upon excitation. Meanwhile, the **1**T composite displays a stronger surface photovoltage response than **1**. This phenomenon could be attributed to the electron transfer between **1** and TiO_2.

Figure 3c shows the energy level diagram of TiO_2 and **1**, which was obtained by the CV and diffuse reflectivity spectra in Figure S5. Because the LUMOs of POMs are formally a combination of d orbits centering on the metal atoms,[56] the LUMO of **1** could be estimated by finding out the applied potential for the first reduction, from which the onset reduction potential was −0.74 V (vs NHE). The CV curve in Figure S6 shows that two anodic peaks were located at 0.73 and 0.96 V, which correspond to the oxidation to Mn^{III} and Mn^{IV} species, respectively, and were accompanied by cathodic peaks at 0.65 and 0.88 V.[57] As a molecular type of semiconductor, the band gap of **1** could be determined by the plot of Kubelka−Munk function F against energy E (Figure S5b),[58] from which an E_g of **1** was estimated as 2.28 eV by the intersection point between the energy axis and the line extrapolated from the linear portion of the absorption edge. Anyway, the electronic characteristic of **1** was achieved in Figure 3c, which was featuring higher LUMO and smaller E_g than TiO_2. These natures render compound **1** the fundamental feasibility to be a potential useful sensitizer for photovoltaic application. Finally, The current−voltage characteristics of **1** sensitized solar cells under simulated AM 1.5 irradiation are shown in Figure 3d. A short-circuit current density (J_{sc}) of 0.745 mA cm^{-2} and an open-circuit voltage (V_{oc}) of 0.423 V were produced with a fill factor (FF) of 0.688, for a power conversion efficiency of 0.22%, whereas a nonsensitized nanocrystalline TiO_2 gave an efficiency of 0.09% (data not shown). On the contrary, the precursor of **1**, $Na_{12}[Mn_4(H_2O)_2(GeW_9O_{34})_2]\cdot 38H_2O$, did not show the positive sensitizing effect, which was possibly due to its lower LUMO (Figure S8) and lack of anchoring group. In conclusion, the sensitization mechanism of **1** could be proposed as in Figure 3c: upon illumination, the electrons in **1** would transfer from HOMO to LUMO, and the excited electrons vectorially flow from **1** toward CB of TiO_2. The remaining holes are further transmitted to the hole transporting material to achieve its sensitizing capability finally.

3.3. Morphologies and Compositions of 1T. Considering the semiconductor-like nature of **1**, and its smaller band gap than TiO_2, a cosensitized solar cell configuration was constructed by N719 sensitized **1** doped TiO_2 photoanode to detect the synergistic effect of **1** and N719 in DSSC. We first prepared a **1**T composite, which was subsequently introduced in the photoanode of DSSC. After sintering and N719 sensitization, **1** and N719 cosensitized configuration was constructed finally. During the experiment, **1** in DMSO solution could strongly adsorb on the surface of TiO_2. When TiO_2 powder was introduced into the DMSO solution of **1**, the bright yellow color of the solution becomes shallow after stirring for a period, and the supernatant absorption spectrum shows significant reduction compared to the original free DMSO solution of **1** after centrifugation, which is shown in Figure S9. This phenomenon indicated that **1**T composite was successfully prepared.

Figure 4 shows the HRTEM images. Figure 4a presents the HRTEM image of a pure P25 sample, which shows irregularly polygonal and spherical particles with sizes ranging from 15 to 50 nm.[59] Compared to the pure P25, the average diameter of the **1**T composite in Figure 5b did not change significantly. However, some TiO_2 particle aggregations exist in the composite. Meanwhile, the surface of the composite was

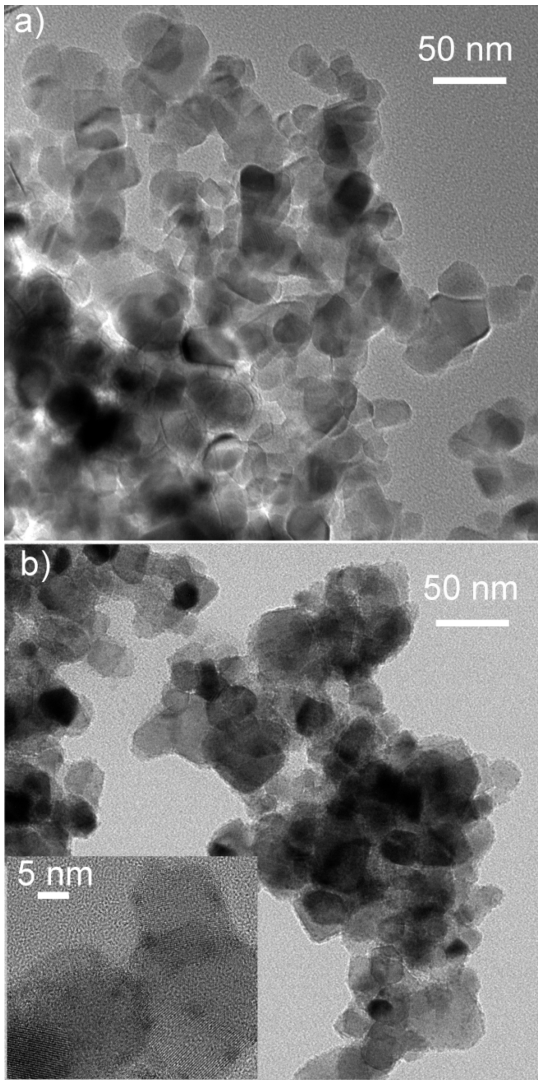

Figure 4. HRTEM images of pure P25 (a) and **1**T composite (b). The inset is the higher magnification image of the **1**T composite.

rougher with many tiny granules dispersing around TiO_2 particles. It can be more clearly seen from the inset of Figure 4b that the size of the granules is about 2 nm, which is very close to the dimension of polyoxoanion **1**. So we speculated that these granules may be the adsorbed polyoxoanions on the surface of TiO_2. Meanwhile, the granules distributed uniformly and have no obvious aggregation, which was essential for POMs to perform effective photoelectric conversion. We further use energy dispersive spectrometry (EDS) to investigate the elemental composition of the composite (Figure S10). Figure S10 shows apparent W element, which further confirmed the adsorption of compound **1** on the TiO_2 surface. Sn and Mn elements were not marked due to their small amount. The thermal stability of **1** was analyzed by its TG curve (Figure S11), which displays that a three step weight loss occurred in the temperature range of 30−652 °C. The former two steps are corresponding to a weight loss of 2.5% and 10.4%, respectively, which are attributed to the loss of water molecules and organic cation $[C(NH_2)_3]^+$ units. The third step after 500 °C was due to the decomposition of the organic tin functional group. This indicated that the organic tin groups remained after sintering at 400 °C, which could still guarantee the integration of TiO_2 and POM. The TG curve has slightly risen after 652 °C, which may be caused by the oxidation of tin in an air atmosphere.

Figure 5 shows the XPS spectra of the as-prepared **1**T composite to show the oxidation state of Ti, W, and Sn atoms. The XPS spectrum for Ti atoms in Figure 5a exhibits two peaks at ca. 458.2 eV in the energy region of $Ti_{2p3/2}$ and ca. 463.9 eV in the energy region of $Ti_{2p1/2}$, which are consistent with the Ti^{IV} oxidation state.[60,61] The binding energy located at 35.0 and 37.0 eV in Figure 5c is attributed to W_{4f} of the POM anions, which is consistent with the W^{VI} oxidation state and suggested that the POM anions existed in the form of the oxidized state.[62] The XPS spectrum for Sn_{3d} (Figure 5d) shows two peaks at ca. 485.9 and 494.3 eV in the energy regions of $Sn_{3d5/2}$ and $Sn_{3d3/2}$, separately, which correspond to the Sn^{IV} oxidation state.[63,64] Figure 5b displays the XPS spectra for O_{1s}. The binding energy located at 529.4 eV is attributed to O^{2-} in the Ti−O bonding.[65] Two other peaks of high binding energy (531.75 and 532.95 eV) were also observed, which are ascribed to O^{2-} in carboxyethyltin group.[66] This result implied the carboxyl of organotin group to be contributed to the adsorption of POM existing in the as-prepared **1**T composite on the surface of TiO_2.

3.4. Performance of DSSCs. After being assembled into the sandwich DSSCs with single N719 sensitized and **1** and N719 cosensitized photoanodes, their performances were investigated under simulated AM 1.5 illumination (100 mW cm^{-2}). All the data of DSSCs were the average of three experimental values, and the absolute deviations were calculated. The photocurrent−voltage (J−V) results in Figure 6a show that the performance of the DSSCs with **1** and N719 cosensitization was enhanced compared to the single N719. The **1**/N719 samples exhibit improved photocurrent (J_{sc} = 12.79 mA cm^{-2}) over N719 samples (J_{sc} = 11.54 mA cm^{-2}). The increase of J_{sc} relates to more photoelectron injection and more efficient charge transfer in the photoanode. Compared with bare TiO_2, **1**-doped TiO_2 could absorb more visible light due to the smaller band gap of **1** than TiO_2, which endowed the cosensitized solar cell with more sunlight absorption. The V_{oc} was also enhanced by the introduction of **1** from 643 mV to 693 mV. This was due to the suppression of electron and hole recombination in cells, which could also be confirmed by the less dark current in **1**/N719 cosensitized solar cells in Figure 6a. In order to detect the performance of the cells under different wavelengths of light, we carried out incident photon conversion efficiency (IPCE) experiment of DSSCs. As depicted in Figure 6b, compared with the DSSCs with single N719 sensitized electrode, the DSSCs using **1**/N719 cosensitized electrode exhibit higher photocurrent conversion efficiency under UV and visible light. This was ascribed to the doping of **1** in TiO_2, which could both utilize more sunlight and accelerate the electron transport in the photoanode.

A dye desorption experiment was carried out to understand the N719 loading on two different electrodes. Two different N719 sensitized electrodes were immersed in 0.1 M NaOH solution and then allowed to stand overnight. The UV/vis spectra of dye solutions desorbed from the two kinds of electrodes were used to characterize the N719 loading, which was shown in Figure S12. As can be seen, almost the same amount of N719 adsorbed on the two kinds of electrodes, indicating that there was little difference in the contribution to the performance of the DSSCs by N719 loading.

In order to better understand the electron transport and carrier recombination behavior in the two kinds of DSSCs, we

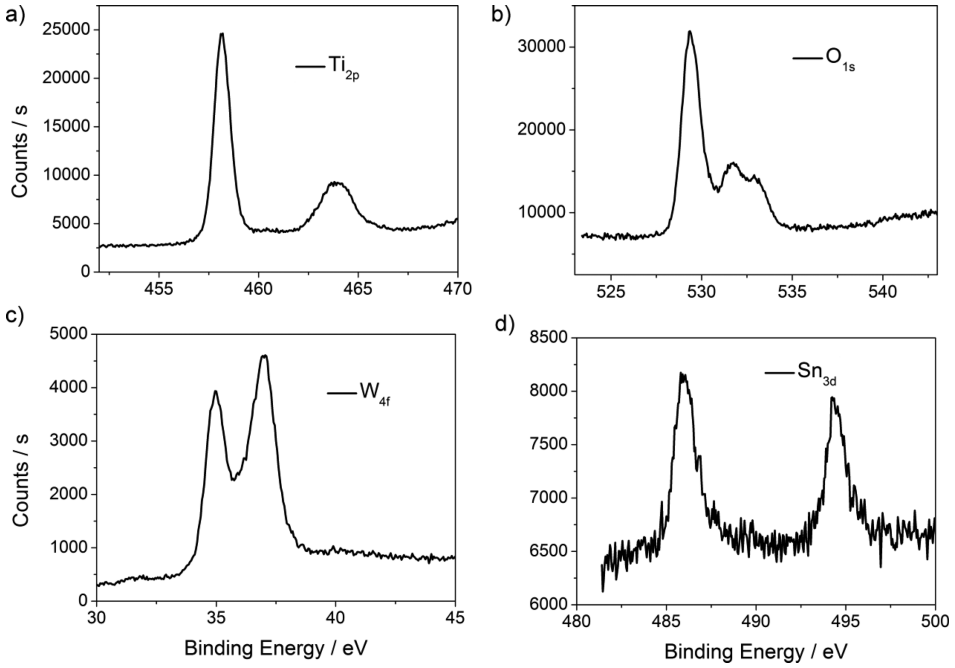

Figure 5. ThXPS spectrum of **1**T composite for (a) Ti_{2p}, (b) O_{1s}, (c) W_{4f}, and (d) Sn_{3d}.

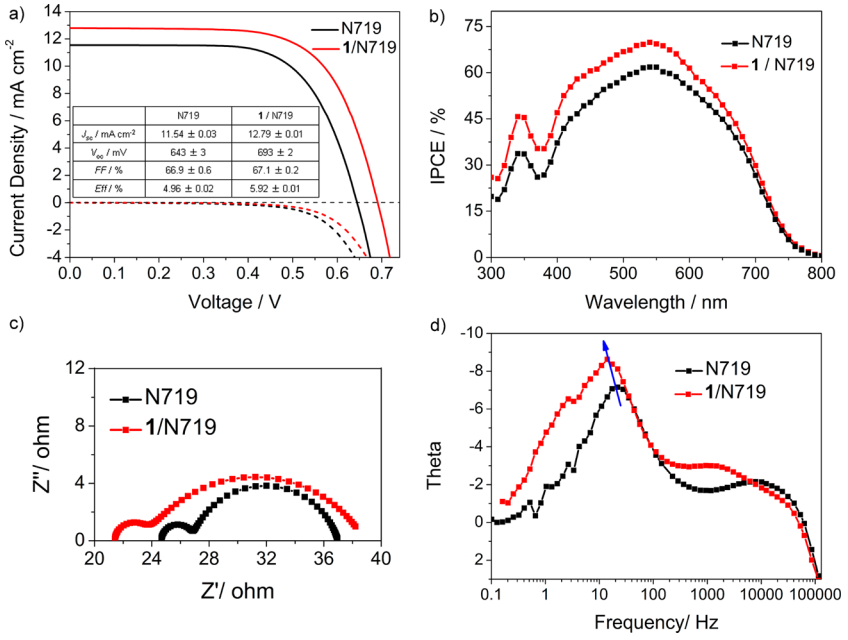

Figure 6. Current−voltage curves under AM 1.5 illumination (solid line) and in the dark (dashed line) of DSSCs with single N719 (dark line) and **1**/N719 (red line) sensitization (a). IPCE for different DSSCs using single N719 (dark line) and **1**/N719 (red line) sensitization (b). The EIS spectra of N719 (dark line) and **1**/N719 (red line)-based DSSCs: Nyquist plots (c). Bode phase plots (d) under AM 1.5 illumination (100 mW cm^{-2}) at a forward bias of the open-circuit voltage with an ac potential amplitude of 10 mV and a frequency range from 0.1 Hz to 100 kHz.

performed electrochemical impedance spectroscopy (EIS) and created an open-circuit voltage decay (OCVD) curve. Figure 6c,d show the EIS result of the DSSCs with single N719 and **1**/N719 cosensitization under AM 1.5 illumination of 100 mW cm^{-2} at a forward bias of the open-circuit voltage with an ac potential amplitude of 10 mV and a frequency range from 0.1 Hz to 100 kHz. The two semicircles from high to low frequency in the Nyquist diagram (Figure 6c) are assigned to the charge-transfer resistance at the interface of the counterelectrode−electrolyte (Rpt) and the charge-transfer resistance occurring at the TiO_2-dye-electrolyte interface (Rct).[67] As shown in Figure 6c, compared with N719 sensitized cells, the **1**/N719 cells have larger Rct. The increase in resistance at the TiO_2-dye-electrolyte interface is beneficial for reducing charge recombination, which could result in smoother electron transfer. Figure 6d shows the Bode phase plots of the EIS result, which displays the frequency peaks of the charge transfer process at different interfaces in DSSCs. From the characteristic low frequency peak, the electron lifetime in the photoanode can be determined by the formula: $\tau_e = \omega_{min}^{-1} = (2\pi f_{max})^{-1}$. The lower frequency in **1**/N719 samples corresponds to the increased τ_e, indicating that **1** could effectively suppress the

dx.doi.org/10.1021/am501192f | ACS Appl. Mater. Interfaces 2014, 6, 7876−7884

recombination of electrons and holes in cells, which was consistent with the result of the dark current−voltage curve.

OCVD analysis was also used to confirm the above result, which monitors the decay of Voc after turning off the illumination in a steady state.[68] The inset in Figure 7 shows

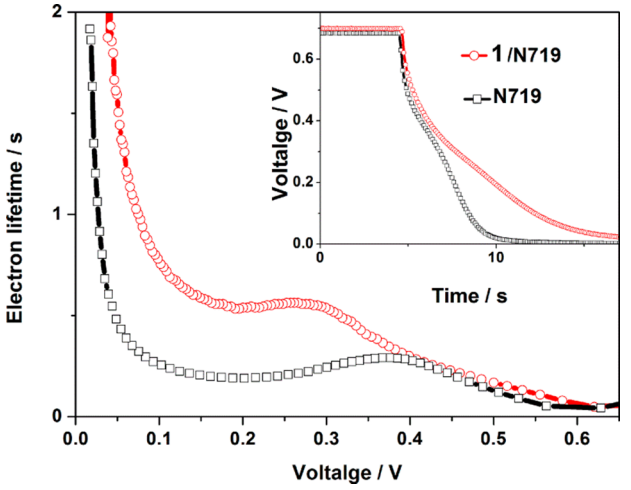

Figure 7. Electron lifetime of DSSCs based on N719 (dark box) and **1**/N719 (red circle) sensitization. The inset is their corresponding OCVD spectra.

the OCVD curves of DSSCs with N719 and **1**/N719 sensitization, and the photovoltage transient spectra demonstrated that Voc decays more slowly for **1**/N719 samples, whereas it decays more quickly for N719 samples. Figure 7 shows the electron lifetime calculated from the OCVD curve, which was obtained by the formula $\tau_e = (kT/e)(dV/dt)^{-1}$. As shown in Figure 7, the electron lifetime in **1**/N719 samples is much larger than in the N719 sample, indicating the variation trend is consistent with the result of EIS analysis.

CONCLUSION

In conclusion, the first open chain carboxyethyltin decorated POM was designed and synthesized, and its semiconductor-like property was investigated by energy level estimation, which shows that it possesses a smaller band gap and higher LUMO than that of TiO_2. An initial examination of compound **1** anchored to nanocrystalline TiO_2 shows that it can function as a sensitizer for a TiO_2-based solar cell. In addition, **1** and N719 cosensitized solar cell configuration was constructed to detect the synergistic effect of **1** and N719, which significantly improved the solar-to-electrical energy conversion efficiency compared with single N719 sensitization. This enhancement was due to both the smaller band gap of **1** than TiO_2 and its role of accelerating electron transmission in the photoanode. These studies show that POMs functionalized by open chain carboxyethyltin could be promising candidates for exploring a new POM-based sensitizer, which will open a new chapter for photoelectrical functionalization of organotin decorated POMs. Future research will focus on synthesizing new carboxyethyltin decorated POMs featuring more visible absorption and employing them to modify TiO_2 in photovoltaic devices.

ASSOCIATED CONTENT

Supporting Information

ORTEP drawing of the polyoxoanion, polyhedral and ball-and-stick view of the 3D supramolecular framework, selected bond lengths (Å) and angles (deg), hydrogen bonds, simulated and experimental XRPD patterns, IR spectrum, CV, and K−M function of **1**; CV of $Na_{12}[Mn_4(H_2O)_2(GeW_9O_{34})_2]\cdot 38H_2O$, the UV−vis spectrum of DMSO solution of **1**, EDS of **1**T, and TG curve of **1**. This material is available free of charge via the Internet at http://pubs.acs.org.

AUTHOR INFORMATION

Corresponding Authors

*E-mail: zhanglancui@lnnu.edu.cn.
*E-mail: chenwl@nenu.edu.cn.
*E-mail: wangeb889@nenu.edu.cn.

Author Contributions

§The manuscript was written through contributions of all authors. All authors have given approval to the final version of the manuscript. These authors contributed equally.

Notes

The authors declare no competing financial interest.

ACKNOWLEDGMENTS

This work was financially supported by the National Natural Science Foundation of China (No. 21131001 and 21201031), Ph. D station Specialized Research Foundation of Ministry of Education for Universities (No. 20120043120007), Science and Technology Development Project Foundation of Jilin Province (No. 201201072), the foundation of China Scholarship Council, and the Analysis and Testing Foundation of Northeast Normal University and the Foundation of Education Department of Liaoning Province (No. L2013414).

REFERENCES

(1) Nazeeruddin, M. K.; Kay, A.; Rodicio, I.; Humphry-Baker, R.; Mueller, E.; Liska, P.; Vlachopoulos, N.; Graetzel, M. Conversion of Light to Electricity by cis-X_2bis(2,2′-bipyridyl-4,4′-dicarboxylate)-ruthenium(II) Charge-Transfer Sensitizers (X = Cl^-, Br^-, I^-, CN^-, and SCN^-) on Nanocrystalline Titanium Dioxide Electrodes. *J. Am. Chem. Soc.* **1993**, *115* (14), 6382−6390.

(2) O'Regan, B.; Gratzel, M. A Low-cost, High-efficiency Solar Cell Based on Dye-Sensitized Colloidal TiO_2 Films. *Nature* **1991**, *353* (6346), 737−740.

(3) Hagberg, D. P.; Yum, J.-H.; Lee, H.; De Angelis, F.; Marinado, T.; Karlsson, K. M.; Humphry-Baker, R.; Sun, L.; Hagfeldt, A.; Grätzel, M.; Nazeeruddin, M. K. Molecular Engineering of Organic Sensitizers for Dye-Sensitized Solar Cell Applications. *J. Am. Chem. Soc.* **2008**, *130* (19), 6259−6266.

(4) Nazeeruddin, M. K.; Zakeeruddin, S. M.; Humphry-Baker, R.; Jirousek, M.; Liska, P.; Vlachopoulos, N.; Shklover, V.; Fischer, C.-H.; Grätzel, M. Acid-Base Equilibria of (2,2′-Bipyridyl-4,4′-dicarboxylic acid)ruthenium(II) Complexes and the Effect of Protonation on Charge-Transfer Sensitization of Nanocrystalline Titania. *Inorg. Chem.* **1999**, *38* (26), 6298−6305.

(5) Cao, Y.; Bai, Y.; Yu, Q.; Cheng, Y.; Liu, S.; Shi, D.; Gao, F.; Wang, P. Dye-Sensitized Solar Cells with a High Absorptivity Ruthenium Sensitizer Featuring a 2-(Hexylthio)thiophene Conjugated Bipyridine. *J. Phys. Chem. C* **2009**, *113* (15), 6290−6297.

(6) Bai, Y.; Zhang, J.; Zhou, D.; Wang, Y.; Zhang, M.; Wang, P. Engineering Organic Sensitizers for Iodine-Free Dye-Sensitized Solar Cells: Red-Shifted Current Response Concomitant with Attenuated Charge Recombination. *J. Am. Chem. Soc.* **2011**, *133* (30), 11442−11445.

(7) Chen, C.; Yang, X.; Cheng, M.; Zhang, F.; Zhao, J.; Sun, L. Efficient Panchromatic Organic Sensitizers with Dihydrothiazole Derivative as π-Bridge for Dye-Sensitized Solar Cells. *ACS Appl. Mater. Interfaces* **2013**, *5* (21), 10960−10965.

(8) Mishra, A.; Fischer, M. K. R.; Bäuerle, P. Metal-Free Organic Dyes for Dye-Sensitized Solar Cells: From Structure: Property Relationships to Design Rules. *Angew. Chem., Int. Ed.* **2009**, *48* (14), 2474−2499.
(9) Santra, P. K.; Kamat, P. V. Mn-Doped Quantum Dot Sensitized Solar Cells: A Strategy to Boost Efficiency over 5%. *J. Am. Chem. Soc.* **2012**, *134* (5), 2508−2511.
(10) Yang, Y.; Zhang, B.; Wang, Y.; Yue, L.; Li, W.; Wu, L. A Photo-driven Polyoxometalate Complex Shuttle and Its Homogeneous Catalysis and Heterogeneous Separation. *J. Am. Chem. Soc.* **2013**, *135* (39), 14500−14503.
(11) Yin, J.; Qi, L.; Wang, H. Polyoxometalate-Assisted Synthesis of TiO_2 Nanoparticles and Their Applications in Aqueous Hybrid Electrochemical Capacitors. *ACS Appl. Mater. Interfaces* **2011**, *3* (11), 4315−4322.
(12) Kim, Y.; Shanmugam, S. Polyoxometalate−Reduced Graphene Oxide Hybrid Catalyst: Synthesis, Structure, and Electrochemical Properties. *ACS Appl. Mater. Interfaces* **2013**, *5* (22), 12197−12204.
(13) Rhule, J. T.; Hill, C. L.; Judd, D. A.; Schinazi, R. F. Polyoxometalates in Medicine. *Chem. Rev.* **1998**, *98* (1), 327−358.
(14) Hou, Y.; Zakharov, L. N.; Nyman, M. Observing Assembly of Complex Inorganic Materials from Polyoxometalate Building Blocks. *J. Am. Chem. Soc.* **2013**, *135* (44), 16651−16657.
(15) Huang, P.; Qin, C.; Su, Z. M.; Xing, Y.; Wang, X. L.; Shao, K. Z.; Lan, Y. Q.; Wang, E. B. Self-Assembly and Photocatalytic Properties of Polyoxoniobates: $\{Nb_{24}O_{72}\}$, $\{Nb_{32}O_{96}\}$, and $\{K_{12}Nb_{96}O_{288}\}$ Clusters. *J. Am. Chem. Soc.* **2012**, *134* (34), 14004−14010.
(16) Yin, P.; Zhang, J.; Li, T.; Zuo, X.; Hao, J.; Warner, A. M.; Chattopadhyay, S.; Shibata, T.; Wei, Y.; Liu, T. Self-Recognition of Structurally Identical, Rod-Shaped Macroions with Different Central Metal Atoms during Their Assembly Process. *J. Am. Chem. Soc.* **2013**, *135* (11), 4529−4536.
(17) Gao, J.; Yan, J.; Beeg, S.; Long, D. L.; Cronin, L. One-Pot versus Sequential Reactions in the Self-Assembly of Gigantic Nanoscale Polyoxotungstates. *J. Am. Chem. Soc.* **2013**, *135* (5), 1796−1805.
(18) Zou, C.; Zhang, Z.; Xu, X.; Gong, Q.; Li, J.; Wu, C. D. A Multifunctional Organic−Inorganic Hybrid Structure Based on Mn^{III}−Porphyrin and Polyoxometalate as a Highly Effective Dye Scavenger and Heterogenous Catalyst. *J. Am. Chem. Soc.* **2012**, *134* (1), 87−90.
(19) Zhao, C.; Huang, Z.; Rodríguez-Córdoba, W.; Kambara, C. S.; O'Halloran, K. P.; Hardcastle, K. I.; Musaev, D. G.; Lian, T.; Hill, C. L. Synthesis and Characterization of a Metal-to-Polyoxometalate Charge Transfer Molecular Chromophore. *J. Am. Chem. Soc.* **2011**, *133* (50), 20134−20137.
(20) Matt, B.; Xiang, X.; Kaledin, A. L.; Han, N.; Moussa, J.; Amouri, H.; Alves, S.; Hill, C. L.; Lian, T.; Musaev, D. G.; Izzet, G.; Proust, A. Long Lived Charge Separation in Iridium(iii)-Photosensitized Polyoxometalates: Synthesis, Photophysical and Computational Studies of Organometallic-Redox Tunable Oxide Assemblies. *Chem. Sci.* **2013**, *4* (4), 1737−1745.
(21) Yamase, T. Photo- and Electrochromism of Polyoxometalates and Related Materials. *Chem. Rev.* **1998**, *98* (1), 307−326.
(22) Zhou, Z.; Zhang, D.; Yang, L.; Ma, P.; Si, Y.; Kortz, U.; Niu, J.; Wang, J. Nona-Copper(ii)-Containing 18-tungsto-8-arsenate(iii) Exhibits Antitumor Activity. *Chem. Commun.* **2013**, *49* (45), 5189−5191.
(23) Kang, Z.; Wang, E.; Gao, L.; Lian, S.; Jiang, M.; Hu, C.; Xu, L. One-Step Water-Assisted Synthesis of High-Quality Carbon Nanotubes Directly from Graphite. *J. Am. Chem. Soc.* **2003**, *125* (45), 13652−13653.
(24) An, H. Y.; Wang, E. B.; Xiao, D. R.; Li, Y. G.; Su, Z. M.; Xu, L. Chiral 3D Architectures with Helical Channels Constructed from Polyoxometalate Clusters and Copper−Amino Acid Complexes. *Angew. Chem., Int. Ed.* **2006**, *45* (6), 904−908.
(25) Tan, H.; Li, Y.; Zhang, Z.; Qin, C.; Wang, X.; Wang, E.; Su, Z. Chiral Polyoxometalate-Induced Enantiomerically 3D Architectures: A New Route for Synthesis of High-Dimensional Chiral Compounds. *J. Am. Chem. Soc.* **2007**, *129* (33), 10066−10067.
(26) Zhang, Z. M.; Li, Y. G.; Yao, S.; Wang, E. B.; Wang, Y. H.; Clérac, R. Enantiomerically Pure Chiral $\{Fe_{28}\}$ Wheels. *Angew. Chem., Int. Ed.* **2009**, *48* (9), 1581−1584.
(27) Fu, H.; Qin, C.; Lu, Y.; Zhang, Z. M.; Li, Y. G.; Su, Z. M.; Li, W. L.; Wang, E. B. An Ionothermal Synthetic Approach to Porous Polyoxometalate-Based Metal−Organic Frameworks. *Angew. Chem., Int. Ed.* **2012**, *51* (32), 7985−7989.
(28) Gómez-Romero, P. Polyoxometalates as Photoelectrochemical Models for Quantum-Sized Colloidal Semiconducting Oxides. *Solid State Ionics* **1997**, *101−103, Part 1* (0), 243−248.
(29) Hiskia, A.; Mylonas, A.; Papaconstantinou, E. Comparison of the Photoredox Properties of Polyoxometallates and Semiconducting Particles. *Chem. Soc. Rev.* **2001**, *30* (1), 62−69.
(30) Wang, J.; Li, H.; Ma, N. N.; Yan, L. K.; Su, Z. M. Theoretical Studies on Organoimido-Substituted Hexamolybdates Dyes for Dye-Sensitized Solar Cells (DSSC). *Dyes Pigm.* **2013**, *99* (2), 440−446.
(31) Wu, K. L.; Ho, S. T.; Chou, C. C.; Chang, Y. C.; Pan, H. A.; Chi, Y.; Chou, P. T. Engineering of Osmium(II)-Based Light Absorbers for Dye-Sensitized Solar Cells. *Angew. Chem., Int. Ed.* **2012**, *51* (23), 5642−5646.
(32) Sun, Z.; Xu, L.; Guo, W.; Xu, B.; Liu, S.; Li, F. Enhanced Photoelectrochemical Performance of Nanocomposite Film Fabricated by Self-Assembly of Titanium Dioxide and Polyoxometalates. *J. Phys. Chem. C* **2010**, *114* (11), 5211−5216.
(33) Anandan, S.; Pitchumani, S.; Muthuraaman, B.; Maruthamuthu, P. Heteropolyacid-Impregnated PVDF as a Solid Polymer Electrolyte for Dye-Sensitized Solar Cells. *Sol. Energy Mater. Sol. Cells* **2006**, *90* (12), 1715−1720.
(34) Park, H.; Choi, W. Photoelectrochemical Investigation on Electron Transfer Mediating Behaviors of Polyoxometalate in UV-Illuminated Suspensions of TiO_2 and Pt/TiO_2. *J. Phys. Chem. B* **2003**, *107* (16), 3885−3890.
(35) Wang, S. M.; Liu, L.; Chen, W. L.; Wang, E. B.; Su, Z. M. Polyoxometalate-Anatase TiO_2 Composites are Introduced into the Photoanode of Dye-Sensitized Solar Cells to Retard the Recombination and Increase the Electron Lifetime. *Dalton Trans.* **2013**, *42* (8), 2691−2695.
(36) Sang, X.; Li, J.; Chen, W.; Wang, E. Polyoxometalate-Assisted Synthesis of the ZnO Polyhedra in an Alkali Solution and Their Photoelectrical Properties. *Mater. Lett.* **2012**, *87* (0), 39−42.
(37) Li, J.; Sang, X.; Chen, W.; Qin, C.; Wang, S.; Su, Z.; Wang, E. The Application of ZnO Nanoparticles Containing Polyoxometalates in Dye-Sensitized Solar Cells. *Eur. J. Inorg. Chem.* **2013**, *2013* (10−11), 1951−1959.
(38) Xin, F.; Pope, M. T. Polyoxometalate Derivatives with Multiple Organic Groups. 1. Synthesis and Structures of Tris(organotin) .beta.-Keggin and.alpha.-Dawson Tungstophosphates. *Organometallics* **1994**, *13* (12), 4881−4886.
(39) Dolbecq, A.; Dumas, E.; Mayer, C. R.; Mialane, P. Hybrid Organic−Inorganic Polyoxometalate Compounds: From Structural Diversity to Applications. *Chem. Rev.* **2010**, *110* (10), 6009−6048.
(40) Kortz, U.; Hussain, F.; Reicke, M. The Ball-Shaped Heteropolytungstates $[\{Sn(CH_3)_2(H_2O)\}_{24}\{Sn(CH_3)_2\}_{12}(A\text{-}XW_9O_{34})_{12}]^{36-}$. *Angew. Chem., Int. Ed.* **2005**, *44* (24), 3773−3777.
(41) Boglio, C.; Micoine, K.; Derat, É.; Thouvenot, R.; Hasenknopf, B.; Thorimbert, S.; Lacôte, E.; Malacria, M. Regioselective Activation of Oxo Ligands in Functionalized Dawson Polyoxotungstates. *J. Am. Chem. Soc.* **2008**, *130* (13), 4553−4561.
(42) Bareyt, S.; Piligkos, S.; Hasenknopf, B.; Gouzerh, P.; Lacôte, E.; Thorimbert, S.; Malacria, M. Highly Efficient Peptide Bond Formation to Functionalized Wells-Dawson-Type Polyoxotungstates. *Angew. Chem., Int. Ed.* **2003**, *42* (29), 3404−3406.
(43) Bareyt, S.; Piligkos, S.; Hasenknopf, B.; Gouzerh, P.; Lacôte, E.; Thorimbert, S.; Malacria, M. Efficient Preparation of Functionalized Hybrid Organic/Inorganic Wells−Dawson-type Polyoxotungstates. *J. Am. Chem. Soc.* **2005**, *127* (18), 6788−6794.
(44) Geisberger, G.; Gyenge, E. B.; Hinger, D.; Bosiger, P.; Maake, C.; Patzke, G. R. Synthesis, Characterization and Bioimaging of

Fluorescent Labeled Polyoxometalates. *Dalton Trans.* **2013**, *42* (27), 9914−9920.
(45) Dupré, N.; Brazel, C.; Fensterbank, L.; Malacria, M.; Thorimbert, S.; Hasenknopf, B.; Lacôte, E. Self-Buffering Hybrid Gold-Polyoxometalate Catalysts for the Catalytic Cyclization of Acid-Sensitive Substrates. *Chem. —Eur. J.* **2012**, *18* (41), 12962−12965.
(46) Zhang, L. C.; Zheng, S. L.; Xue, H.; Zhu, Z. M.; You, W. S.; Li, Y. G.; Wang, E. New Tetra(organotin)-Decorated Boat-Like Polyoxometalate. *Dalton Trans.* **2010**, *39* (14), 3369−3371.
(47) Zhang, L. C.; Xue, H.; Zhu, Z. M.; Wang, Q. X.; You, W. S.; Li, Y. G.; Wang, E. B. New Estertin Derivatives Based on Trivacant Keggin-Type $[\beta\text{-}SbW_9O_{33}]^{9-}$ Cluster. *Inorg. Chem. Commun.* **2010**, *13* (5), 609−612.
(48) Wang, Z. J.; Zhang, L. C.; Zhu, Z. M.; Chen, W. L.; You, W. S.; Wang, E.-B. Two New Sandwich-Type Tungstobismuthates Constructed from Trivacant Keggin Units, Estertin and Transition Metals. *Inorg. Chem. Commun.* **2012**, *17* (0), 151−154.
(49) Yang, H.; Zhang, L. C.; Yang, L.; Zhang, X. L.; You, W. S.; Zhu, Z. M. Synthesis, Characterization and Catalytic Activity of a New Sandwich-Type Tungstophosphate Functionalized by Carboxyethyltin. *Inorg. Chem. Commun.* **2013**, *29* (0), 33−36.
(50) Kortz, U.; Nellutla, S.; Stowe, A. C.; Dalal, N. S.; Rauwald, U.; Danquah, W.; Ravot, D. Sandwich-Type Germanotungstates: Structure and Magnetic Properties of the Dimeric Polyoxoanions $[M_4(H_2O)_2(GeW_9O_{34})_2]^{12-}$ (M = Mn^{2+}, Cu^{2+}, Zn^{2+}, Cd^{2+}). *Inorg. Chem.* **2004**, *43* (7), 2308−2317.
(51) Hutton, R. E.; Burley, J. W.; Oakes, V. β-substituted alkyltin halides: I. Monoalkyltin trihalides: Synthetic, Mechanistic and Spectroscopic aspects. *J. Organomet. Chem.* **1978**, *156* (2), 369−382.
(52) Ito, S.; Chen, P.; Comte, P.; Nazeeruddin, M. K.; Liska, P.; Péchy, P.; Grätzel, M. Fabrication of Screen-Printing Pastes from TiO_2 Powders for Dye-Sensitised Solar Cells. *Prog. Photovoltaics* **2007**, *15* (7), 603−612.
(53) Sheldrick, G. M. *SHELXL 97*; University of Göttingen: Göttingen, Germany, 1999.
(54) Desilvestro, J.; Graetzel, M.; Kavan, L.; Moser, J.; Augustynski, J. Highly Efficient Sensitization of Titanium Dioxide. *J. Am. Chem. Soc.* **1985**, *107* (10), 2988−2990.
(55) Luo, X.; Li, F.; Xu, B.; Sun, Z.; Xu, L. Enhanced Photovoltaic Response of the First Polyoxometalate-Modified Zinc Oxide Photoanode for Solar Cell Application. *J. Mater. Chem.* **2012**, *22* (30), 15050−15055.
(56) Lopez, X.; Carbo, J. J.; Bo, C.; Poblet, J. M. Structure, Properties and Reactivity of Polyoxometalates: A Theoretical Perspective. *Chem. Soc. Rev.* **2012**, *41* (22), 7537−7571.
(57) Liu, J.; Ortega, F.; Sethuraman, P.; Katsoulis, D. E.; Costello, C. E.; Pope, M. T. Trimetallo Derivatives of Lacunary 9-Tungstosilicate Heteropolyanions. Part 1. Synthesis and Charaterization. *Dalton. Trans.* **1992**, *12*, 1901−1906.
(58) Zhai, Q. G.; Wu, X. Y.; Chen, S. M.; Zhao, Z. G.; Lu, C. Z. Construction of Ag/1,2,4-Triazole/Polyoxometalates Hybrid Family Varying from Diverse Supramolecular Assemblies to 3-D Rod-Packing Framework. *Inorg. Chem.* **2007**, *46* (12), 5046−5058.
(59) Wang, H.; Wu, Y.; Xu, B.-Q. Preparation and Characterization of Nanosized Anatase TiO_2 Culloids for Photocatalysis. *Appl. Catal., B* **2005**, *59* (3−4), 139−146.
(60) Fierro, J. L. G.; Arrua, L. A.; Lopez Nieto, J. M.; Kremenic, G. Surface Properties of Co-precipitated VTiO Catalysts and Their Relation to the Selective Oxidation of Isobutene. *Appl. Catal.* **1988**, *37* (0), 323−338.
(61) Galuska, A. A.; Uht, J. C.; Marquez, N. Reactive and Nonreactive Ion Mixing of Ti Films on Carbon Substrates. *J. Vac. Sci. Technol., A* **1988**, *6* (1), 110−122.
(62) Xu, L.; Zhang, H.; Wang, E.; Kurth, D. G.; Li, Z. Photoluminescent Multilayer Films Based on Polyoxometalates. *J. Mater. Chem.* **2002**, *12* (3), 654−657.
(63) Willemen, H.; Wuyts, L. F.; van de Vondel, D. F.; van der Kelen, G. P. ESCA and IR Study of Cyclopentadienyl Tungsten and Molybdenum Carbonyl Compounds. *J. Electron Spectrosc. Relat. Phenom.* **1977**, *11* (3), 245−250.
(64) Shiratsuchi, R.; Hongo, K.; Nogami, G.; Ishimaru, S. Reduction of CO_2 on Fluorine−Doped SnO_2 Thin-Film Electrodes. *J. Electrochem. Soc.* **1992**, *139* (9), 2544−2549.
(65) Sleigh, C.; Pijpers, A. P.; Jaspers, A.; Coussens, B.; Meier, R. J. On the Determination of Atomic Charge Via ESCA Including Application to Organometallics. *J. Electron Spectrosc. Relat. Phenom.* **1996**, *77* (1), 41−57.
(66) Bournel, F.; Laffon, C.; Parent, P.; Tourillon, G. Adsorption of Some Substituted Ethylene Molecules on Pt(111) at 95 K Part 1: NEXAFS, XPS and UPS studies. *Surf. Sci.* **1996**, *350* (1−3), 60−78.
(67) Wang, Q.; Moser, J.-E.; Grätzel, M. Electrochemical Impedance Spectroscopic Analysis of Dye-Sensitized Solar Cells. *J. Phys. Chem. B* **2005**, *109* (31), 14945−14953.
(68) Bisquert, J.; Zaban, A.; Greenshtein, M.; Mora-Seró, I. Determination of Rate Constants for Charge Transfer and the Distribution of Semiconductor and Electrolyte Electronic Energy Levels in Dye-Sensitized Solar Cells by Open-Circuit Photovoltage Decay Method. *J. Am. Chem. Soc.* **2004**, *126* (41), 13550−13559.